Collisionless shock experiments with lasers and observation of Weibel instabilitiesa)

H.-S. Park, C. M. Huntington, F. Fiuza, R. P. Drake, D. H. Froula, G. Gregori, M. Koenig, N. L. Kugland, C. C. Kuranz, D. Q. Lamb, M. C. Levy, C. K. Li, J. Meinecke, T. Morita, R. D. Petrasso, B. B. Pollock, B. A. Remington, H. G. Rinderknecht, M. Rosenberg, J. S. Ross, D. D. Ryutov, Y. Sakawa, A. Spitkovsky, H. Takabe, D. P. Turnbull, P. Tzeferacos, S. V. Weber, and A. B. Zylstra

Citation: Physics of Plasmas (1994-present) **22**, 056311 (2015); doi: 10.1063/1.4920959
View online: http://dx.doi.org/10.1063/1.4920959
View Table of Contents: http://scitation.aip.org/content/aip/journal/pop/22/5?ver=pdfcov
Published by the AIP Publishing

Collisionless shock experiments with lasers and observation of Weibel instabilities[a)]

H.-S. Park,[1,b),c)] C. M. Huntington,[1] F. Fiuza,[1] R. P. Drake,[2] D. H. Froula,[3] G. Gregori,[4] M. Koenig,[5] N. L. Kugland,[6] C. C. Kuranz,[2] D. Q. Lamb,[7] M. C. Levy,[1] C. K. Li,[8] J. Meinecke,[4] T. Morita,[9] R. D. Petrasso,[8] B. B. Pollock,[1] B. A. Remington,[1] H. G. Rinderknecht,[8] M. Rosenberg,[3] J. S. Ross,[1] D. D. Ryutov,[1] Y. Sakawa,[9] A. Spitkovsky,[10] H. Takabe,[9] D. P. Turnbull,[1] P. Tzeferacos,[7] S. V. Weber,[1] and A. B. Zylstra[8]
[1]*Lawrence Livermore National Laboratory, Livermore, California 94550, USA*
[2]*University of Michigan, Ann Arbor, Michigan 48109, USA*
[3]*Laboratory for Laser Energetics, University of Rochester, Rochester, New York 14636, USA*
[4]*University of Oxford, Parks Road, Oxford OX1 3PU, United Kingdom*
[5]*LULI, Ecole Polytechnique, Palaiseau, France*
[6]*Lam Research Corporation, Fremont, California 94538, USA*
[7]*University of Chicago, Chicago, California 94538, USA*
[8]*Massachusetts Institute of Technology, Cambridge, Massachusetts 02139, USA*
[9]*Institute of Laser Engineering, Osaka University, Osaka 565-0871, Japan*
[10]*Princeton University, Princeton, New Jersey 08544, USA*

(Received 23 December 2014; accepted 6 March 2015; published online 13 May 2015)

Astrophysical collisionless shocks are common in the universe, occurring in supernova remnants, gamma ray bursts, and protostellar jets. They appear in colliding plasma flows when the mean free path for ion-ion collisions is much larger than the system size. It is believed that such shocks could be mediated via the electromagnetic Weibel instability in astrophysical environments without pre-existing magnetic fields. Here, we present laboratory experiments using high-power lasers and investigate the dynamics of high-Mach-number collisionless shock formation in two interpenetrating plasma streams. Our recent proton-probe experiments on Omega show the characteristic filamentary structures of the Weibel instability that are electromagnetic in nature with an inferred magnetization level as high as ~1% [C. M. Huntington *et al*., "Observation of magnetic field generation via the weibel instability in interpenetrating plasma flows," Nat. Phys. **11**, 173–176 (2015)]. These results imply that electromagnetic instabilities are significant in the interaction of astrophysical conditions. © *2015 AIP Publishing LLC*. [http://dx.doi.org/10.1063/1.4920959]

I. INTRODUCTION

Astrophysical collisionless shocks have been of interest as a mechanism for self-generating magnetic fields and cosmic-ray acceleration. Collisionless shocks are formed from plasma instabilities when the Coulomb mean-free-path for ion-ion collisions is much larger than the system size. These conditions occur in many astrophysical objects, both relativistic and non-relativistic including supernova remnants and gamma-ray bursts. It has been recently proposed[2–6] that the generation of magnetic fields can occur in these shocks on cosmologically-fast timescales, via the Weibel instability.[7] Three-dimensional (3D) particle-in-cell (PIC) numerical simulations have confirmed that the strength and scale of Weibel-generated magnetic fields are consistent with what would be required to play a dominant role in the magnetization of astrophysical collisionless shocks.[8–13] Thus, the Weibel instability can convert kinetic energy to magnetic energy to provide seed magnetic fields for the universe.[7]

Figure 1 shows the concept for Weibel mediated shock formation, in the case where the Weibel instabilities are created from a momentum anisotropy in the distribution of the plasma flows,[7] creating localized self-generated magnetic fields. The self-generated magnetic fields trap ions via the Lorenz force, thereby imitating collisions in the usual collisional shocks and leading to collisionless shock formation. The signature of the instability is a pattern of current filaments stretched along the axis of symmetry of the flows. The exact understanding of the required physical conditions for such an occurrence has not been well characterized. Laboratory laser experiments can provide a unique platform for studying electromagnetic Weibel instabilities that occur in high-Mach number plasma flows. There have been many attempts to create collisionless shocks in the laboratory, but most of them only formed electrostatic shocks. Very recently, very high intensity lasers such as Omega and the National Ignition Facility (NIF) have come on-line and are capable of creating the conditions required for the observation of electromagnetic Weibel instabilities.[1,14,15]

The conditions required to create collisionless shocks are: (1) The collision mean-free path λ_{mfp} for the more higher Z ion component (carbon, in the case of CH plasmas) should be much larger than the system size (that is, the spatial scale of the interacting flows, l_{int}): $\lambda_{mfp} \gg l_{int}$; (2) the system size, l_{int}, must be much larger than the instability scale length, l^* : $l_{int} \gg l^*$.[16–18] So, we are looking for conditions where

[a)]Paper BI2 2, Bull. Am. Phys. Soc. **59**, 25 (2014).
[b)]Invited speaker.
[c)]Electronic mail: park1@llnl.gov

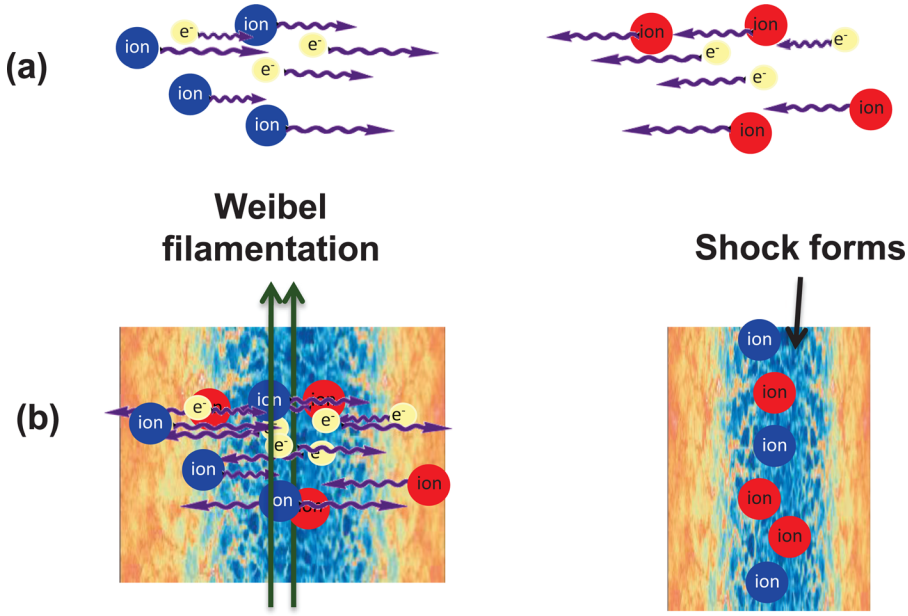

FIG. 1. Conceptual sketch of collisionless shock forming process. The high velocity plasma flows have large Coulomb mean free path where clean penetration is expected. The Weibel instability can create local magnetic field that traps the ions via $q \times \mathbf{B}$ Lorenz force and creates a shock.

$$l^* \ll l_{int} \ll \lambda_{mfp}. \tag{1}$$

Assuming that the temperature of the colliding flows is much smaller than the ion energy due to the bulk flow velocity, λ_{mfp} can be calculated by[19]

$$\lambda_{mfp}\,[cm] \sim 5 \times 10^{-13} \frac{A_Z^2}{Z^4} \frac{(v\,[cm/s])^4}{n_z\,[cm^{-3}]}, \tag{2}$$

where A_Z, Z, and n_Z are the atomic weight, charge, and number density of the main ion component, and v is the flow bulk velocity before the collision with the other flow.

When evaluating the plasma instability scale length, l^*, we consider the electrostatic instabilities and electromagnetic instabilities, separately. Electrostatic plasma instability length, l^*_{ES}, is estimated with a model that is based on the growth-rate assessments in Ref. 20

$$l^*_{ES} \sim K \frac{v}{\omega_{pi}} \frac{W}{T_e}, \tag{3}$$

where $K \gg 1$ is a numerical factor accounting for the number of the growth times required for the instability to reach a developed stage, W is the kinetic energy of the main ion component in the flow, T_e is the electron temperature (in energy units) in the flow prior to the collision, v is the bulk flow velocity, and ω_{pi} is the ion plasma frequency. Note that v/ω_{pi} is roughly the distance travelled by the flow in one ion plasma wave oscillation period. Hence, $K \gg 1$ implies that the plasma in the interaction region should correspond to many ($\gg$1) plasma wavelengths. With

$$W[eV] = 5.2 \times 10^{-13} A_z (v\,[cm/s])^2, \tag{4}$$

l^*_{ES} evaluates to

$$l^*_{ES}\,[cm] \sim 10^{-3} K \frac{v\,[cm/s]\sqrt{A_Z}}{Z\sqrt{n_Z[cm^{-3}]}} \frac{W\,[eV]}{T_e\,[eV]}. \tag{5}$$

The scale length of the electromagnetic instability, l^*_{EM}, of the Weibel type can be written as

$$l^*_{EM} \approx K' \frac{c}{\omega_{pi}}, \quad \text{where } K' > 1. \tag{6}$$

Here, c/ω_{pi} corresponds to the ion plasma skin depth, namely, the distance light could travel in one ion plasma wave oscillation period. The factor K' indicates the level of required ion skin depth to fully form a shock. PIC simulations indicate that K′ should be of the order of 300.[21] In counter-streaming plasma experiments, the electrostatic instability is expected to be dominant at the initial stage of interaction before saturating as the Weibel instability develops.[12] Comparing Eqs. (5) and (6) to Eq. (2), the optimum conditions for the study of collisionless shocks favor higher flow energies and electron temperatures, and lower flow densities. Lower-Z materials are somewhat preferable as λ_{mfp} very rapidly increases for lower Z.

In the experiments with two counter-streaming plasmas, there may exist a strong difference in the collisionality between ions of the two streams and the ion collisionality within each stream (intra-stream collisionality.[18]) The collisions of the ions of one stream with the ions of the other stream have typically a large collision length, due to the high energy of the relative motion. Conversely, the collisions within each stream are determined by a relatively low ion temperature. As the electron thermal velocity is much higher than the flow velocity, the electron scattering on the ions is determined by the electron temperature and total ion density. So, in determining whether the interaction is truly collisionless, or not, it is desirable to characterize these types of collisions as well. As an illustration, we provide Table I where the corresponding frequencies and free-path lengths are presented for a range of possible parameters of the interacting streams. The total (between the two streams) electron density is $10^{19}\,cm^{-3}$; the velocity of each stream is 10^8 cm/s; streams of fully ionized carbon (Z = 6) are considered. The temperatures in the table are given in the units of keV. Column 2

TABLE I. Intra-stream collisions in fully ionized carbon streams.

(keV)	ν_{ZZ}, s^{-1}	ν_{eZ}, s^{-1}	$(v/c)\omega_{pi}$, s^{-1}
$T_e=0.25; T_i=0.15$	8×10^{10}	4.3×10^{11}	9×10^{9}
$T_e=0.5; T_i=0.3$	3×10^{10}	1.8×10^{11}	9×10^{9}
$T_e=T_i=1$	8×10^{9}	1.8×10^{10}	9×10^{9}
$T_e=T_i=2$	3×10^{9}	7×10^{9}	9×10^{9}

represents intra-stream ion-ion collisions; column 3—the electron scattering frequency on the ions; and column 4—the maximum (over wave numbers) possible growth rate.

Frequent intra-stream collisions affect the particle response to electromagnetic perturbations: the collisionless response (in particular, Landau damping) is replaced by the hydrodynamical response. This may affect the particle acceleration. There is also an effect on the linear growth-rate that becomes lower than the reference growth rate (last column in Table I), see Ref. 22. The general conclusion from this discussion is that experiments on the collisionless Weibel instability should be done at as high electron and ion temperatures as possible, albeit still well below the ion kinetic energy in each stream (which is 60 keV for the parameters discussed in Table I).

II. EXPERIMENTAL SETUP

Figure 2 shows our typical laser experimental configuration at the Omega laser facility.[23] Two face-on polyethylene (CH_2) plastic foils are heated by 8 beams, ~4 kJ, of 351 nm laser energy with focal spot diameters of 250 μm on the target surface with an incidence angle of 50 deg. An overlap zone on the target was approximately a circle with diameter of ~300 μm. The pulse length was 1 ns, and the intensity within this circle was $\sim2\times10^{15}$ W/cm^2. The separation is 8 mm between the targets. This setting, due to a nearly axial symmetry, should have produced two conically-divergent high-velocity counter-streaming flows.

In order to verify that we meet the condition of collisionless regime imposed in Eq. (1), we extensively studied the plasma state of the single and double flows using Thomson scattering (TS).[24] Thomson scattering is used to measure the plasma bulk velocity (v), electron temperature (T_e), ion temperature (T_i), and electron density (n_e), For our experiments, the probe laser of 526.5 nm studies a plasma volume of 100 μm × 100 μm × 60 μm at the central region of the counter-streaming plasmas. Thomson scattered light is measured for two spectral ranges, a large spectral range to measure the electron feature (collective scattering from electron-plasma waves) and a narrow spectral range to measure the ion feature (collective scattering from ion-acoustic waves). An example of time composite electron and ion features from the double foil counter-streaming data is shown in the top right panel in Fig. 2.

Extensive Thomson scattering data were collected for both single-flows and counter-streaming flows. Time-slices of the data from the electron feature are then fitted with the Thomson scattering form-factor allowing a measurement of the electron temperature (T_e) and electron density (n_e). With constraints from the electron feature fitting, the ion feature can then be used to measure the ion temperature (T_i) and bulk plasma flow velocity (v). This can be understood from the simplified dispersion relation, $\Delta\lambda = \frac{4\lambda_{probe}}{c}\sin(\theta/2)\sqrt{\frac{ZT_e}{M}+\frac{3T_i}{M}}$. The details of these measurements can be found in Refs. 17 and 25.

Our detailed measurements indicate that the bulk flow velocity is >1000 km/s up to 5 ns and is not suppressed for the double flow case, indicating interpenetrating flows as seen in Figure 3(a). The single flow n_e is $\sim5\times10^{18}$ cm^{-3} at maximum and is doubled for the counter-streaming case at 1×10^{19} cm^{-3} (Figure 3(b)). This indicates that a shock is not quite formed, as we should expect a factor of >2 increase in electron and ion densities at a shock front. Another compelling finding from the TS measurement is the significant increase in T_e (Figure 3(c)) and T_i (Figure 3(d)) for the counter-streaming double flows. The electron temperature, T_e, was ~200 eV for the single-flow case, whereas in the double-flow case, the electron temperature reached nearly 1 keV. The rapid T_e increase at early time is explained by electron-ion collisions from ion slowing-down by drag forces

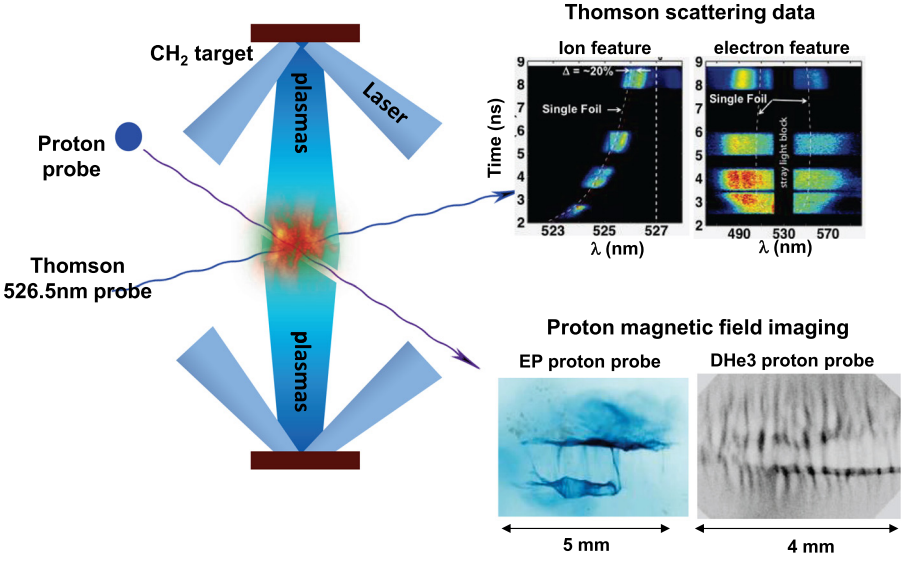

FIG. 2. Schematic of Omega experiment. We use Thomson scattering to probe the plasma state and proton probe to image the magnetic field structures.

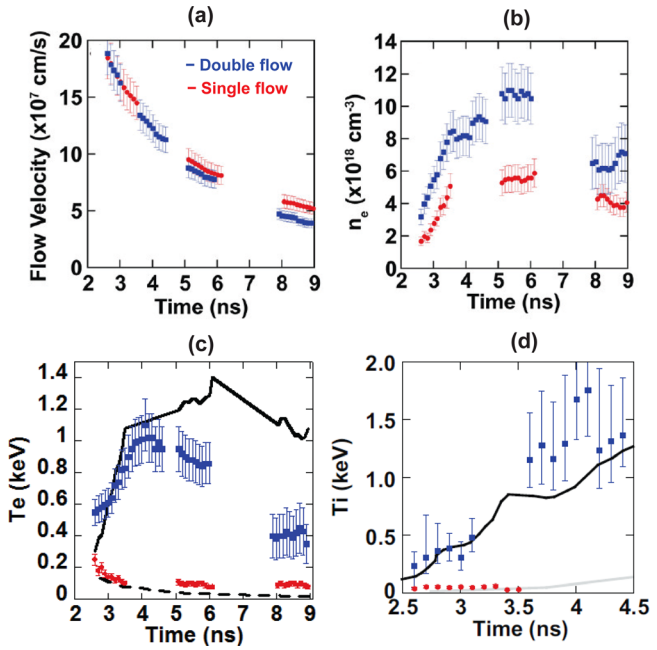

FIG. 3. Plasma parameters measured by the Thomson scattering of single and double flows: (a) flow velocity; (b) electron density; (c) electron temperature; and (d) ion temperature. Reprinted with permission from Phys. Plasmas **19**, 056501 (2012). Copyright 2012 AIP Publishing LLC.

caused by the 'resting' electron gas.[18] While this drag-force model explained the T_e increase very well, the ion-ion collisions could not explain the observed T_i increase. When PIC simulations that included collisional effects are applied accounting for acoustic two-stream electrostatic instabilities, we are able to reproduce the T_i increase. This instability occurs for $T_e > T_i$ and therefore leads to the heating of the ions to temperatures close to T_e. Our quantitative plasma state measurements suggest that the intra-flow ion and electron collisional effects are important and that inter-flow ion collisions are rare from high velocity flows.

Using the measured plasma parameters, l^*_{EM}, l^*_{ES}, l_{int}, and λ_{mfp} are calculated using the equations above. As shown in Figure 4, λ_{mfp} is much larger than the instability unit scale lengths demonstrating that we are in collisionless regime.

In our experiments, the magnetic field structure of the forming collisionless shock is characterized using proton probes. We use two different proton sources: (1) short pulse generated protons by the target-normal sheath acceleration mechanism;[26] and (2) imploding a capsule filled with deuterium (D) and helium-3 (^{3}He) fuel.[27] The short pulse generated protons are generated by illuminating a 10 ps pulse of up to 800 J of 1053 nm infrared light onto a 40 μm diameter spot for an intensity of $\sim 2 \times 10^{18}$ W/cm^2 on an Au disk target.[28,29] Electric and magnetic fields deflect the protons which are then recorded on radiochromic film layered with Al filters to obtain a range of proton energies from 5 to 15 MeV.

We also use the 14.7 MeV and 3 MeV mono-energetic proton source generated by thermonuclear interactions of D+^{3}He $\rightarrow$ ^{4}He + p (14.7 MeV) and D + D $\rightarrow$ t + p (3 MeV).[30] For our experiments, the 2 μm thin silica capsules are filled with 18 atm D^{3}He fuel (6 atm of D and 12 atm of ^{3}He for equal atomic distribution) and are compressed uniformly by

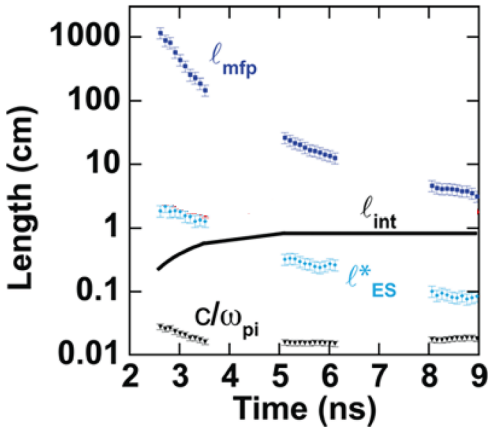

FIG. 4. Coulomb mean free paths and instability scale lengths by Eqs. (5) and (6). Reprinted with permission from Phys. Plasmas **19**, 056501 (2012). Copyright 2012 AIP Publishing LLC.

$\sim$9 kJ of laser energy from 18 laser beams. The protons are generated at shock convergence creating $\sim 10^8$ protons isotropically lasting $\sim$50 ps with a source size of $\sim$50 μm in diameter. A 10 $\times$ 10 cm CR-39 detector pack was placed 27 cm from the object plane for a magnification M = 27 and a 3.7 mm field of view. The pack consists of two layered and filtered pieces of 1.5 mm thick CR-39; the first piece detects the DD-p and has a 12.5 μm thick Ta filter while the second piece has an additional 150–200 μm Al filter and detects the D^{3}He capsule-produced protons. The filtering serves to eliminate laser-generated fast ions and to range the protons to an optimal energy for the CR-39 detector.[31] Each piece of CR-39 is etched in a NaOH solution to reveal the proton tracks and then scanned on a microscope system, which records the location and characteristics of each particle track. In the analysis, limits on the contrast, eccentricity, and diameter of tracks are chosen to reject background. The images displayed are a fluence histogram of the resulting signal counts with a bin size of 333 μm at the detector plane, which was chosen for high resolution with adequate statistics per bin. Examples of these two proton magnetic field imaging are shown in the right-bottom panel in Figure 2.

III. OBSERVATION OF SELF-ORGANIZING FIELDS USING SHORT PULSE GENERATED PROTON SOURCE

Using proton probes generated by short pulse lasers on EP, we observe large, stable, reproducible electromagnetic field structures that arise in counter-streaming, interpenetrating, supersonic plasma flows in the laboratory. These large-scale features are produced when energy is transferred from smaller to larger scales. The structures are predominantly oriented transverse to the primary flow direction, extend for much larger distances than the intrinsic plasma spatial scales, and persist for much longer than the plasma kinetic timescales. We observe that this structure lasts >5 ns, whereas our plasma condition indicates that ion-kinetic timescale is $2\pi/\omega_{pi} \sim 1.1$ ps and the electron-kinetic timescale is $2\pi/\omega_{pe} \sim 40$ fs. One such example image is shown in Figure 5(a). This image is

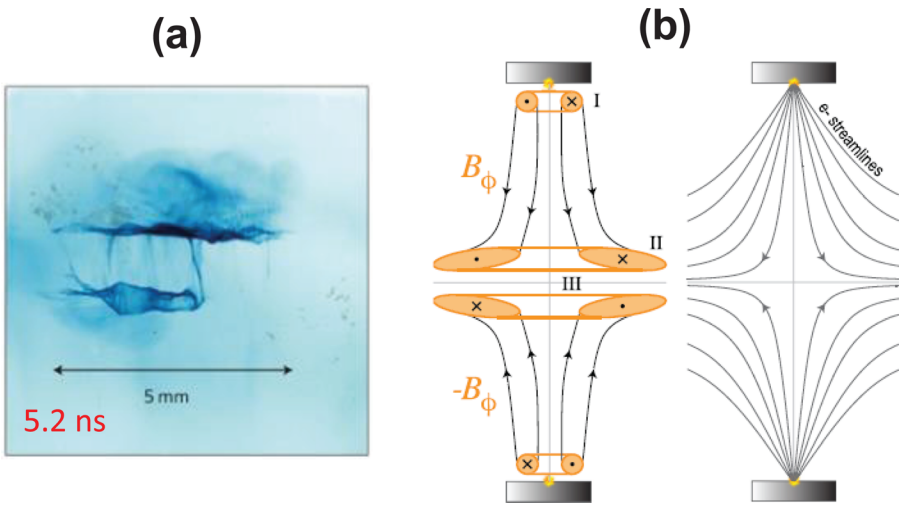

FIG. 5. (a) Omega EP short pulse generated proton image of counter-streaming plasmas at 5.2 ns after the laser. Highly stable self-organizing planar magnetic field structures are observed. (b) This is from the Biermann battery magnetic field that is generated near the target surface; advects along the electron flows; then recompress in the mid-plane. Reprinted with permission from Phys. Plasmas **20**, 056313 (2013). Copyright 2013 AIP Publishing LLC.

taken at 5.2 ns after the laser, when sharp co-planar field structures are clearly visible.

Their origin is now explained by the magnetic field advection process. Here, the Biermann battery magnetic field is generated near the target surface in a toroidal shape, and advects along the electron plasma flows, then recompresses near the midplane.[3] The magnetic field strength is evaluated by the caustic analysis by[32]

$$B_{cf} = \frac{m_p c}{el}\sqrt{\frac{2W}{m_p}}\frac{d^3}{\sqrt{\pi}a^2 \sin\psi}, \tag{7}$$

where W is the proton kinetic energy (8.8 MeV), b/a—the aspect ratio (1/20), ψ is the distance from proton source to object plane (8 mm), and ψ is the tilt angle of the plane (5 to 10 degrees). When we apply our experimental measurements and observables, we derive $B_0 = 10$ Tesla. While this kind of self-organizing structures may play an important role in astrophysical conditions, we find that the magnetic field generation from this Biermann battery source is small compared to the Weibel source.

IV. OBSERVATION OF WEIBEL FILAMENTATION USING D^{3}He CAPSULE GENERATED PROTON SOURCE

Electromagnetic fields of the counter-streaming flows are imaged with protons generated by a D^{3}He imploding capsule. The advantage of the D^{3}He capsule generated protons are their mono-energetic properties at 14.7 MeV and 3 MeV sources and the high flux. Figure 6 shows the comparison of proton radiography image between the single flow and the counter-streaming double flows. The targets were diagonal in these images as depicted in the Figure. Strong striations in the counter-streaming double flow images are obvious along with the co-planar structures, indicating that plasma instabilities created strong electromagnetic features. The filaments are likely from the Weibel induced fields, whereas the co-planar features are the Biermann field recompression described in Sec. III.

Figure 7 shows the compilation of the filament evolution taken over several shots including repeats. We observe a gradual increase in the spatial scale, in qualitative agreement with the growth-rate dependence on the wavelength (the shortest develop first).

To quantify the change in observed filament spacing, rectangular sections of the images are integrated to create radial intensity profiles. To highlight the regions of the images where there is an absence of protons, the intensity I is modified as: $f(I) = \langle I\rangle - I$, where $\langle I\rangle$ is the mean pixel value over the entire region of interest. Peaks in this profile are identified, and their relative spacing in the target plane is recorded (Fig. 8(a)). This method is applied at several locations in the image, and the measured spacing between filaments is binned for all regions.

The distribution of filament spacing is fit by a function of the form

$$f(x|k,\mu,\sigma_w) = \left(\frac{1}{\sigma_w}\right)\exp\left(-\left(1+k\frac{(x-\mu)}{\sigma_w}\right)^{-\frac{1}{k}}\right) \times \left(1+k\frac{(x-\mu)}{\sigma_w}\right)^{-1-\frac{1}{k}}, \tag{8}$$

where shape, scale, and location parameters k, σ_w, and μ are fit according to the data (This is probability distribution function of the generalized extreme value distribution). This

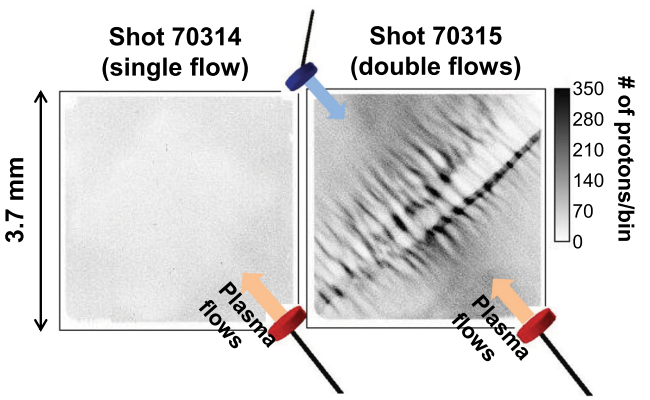

FIG. 6. D^{3}He proton backlighter (14.7 MeV) radiographed the electromagnetic field structures in the middle of the counter-streaming plasma flows. Strong striation features are observed.

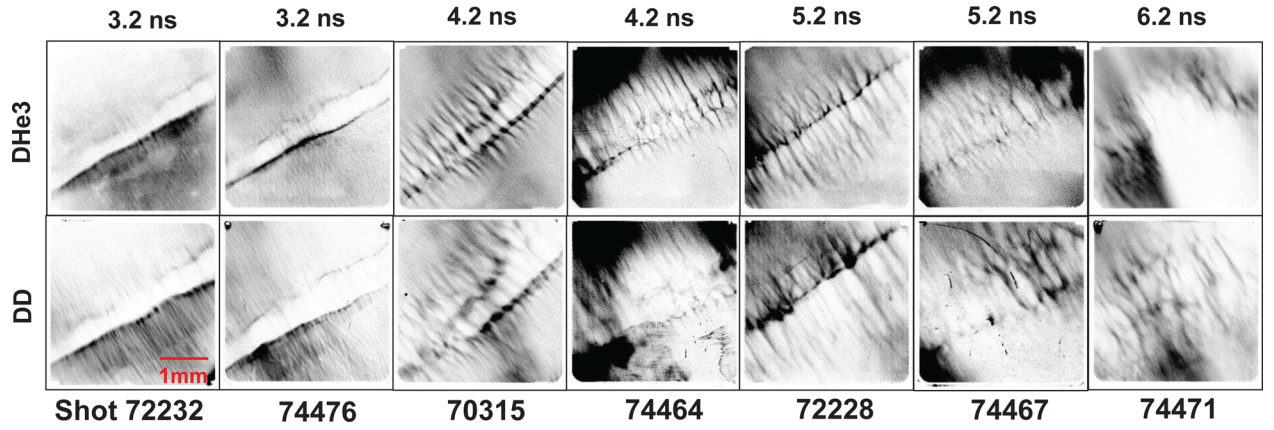

FIG. 7. Compilation of proton radiography images taken over several shots and different timings. We have repeated a set to see the repeatability of filament evolution.

distribution captures the observed filament spacing, which generally skews positive. In Figure 8(b), the measured filament spacing is shown, and quantified by μ in Eq. (8). Note that in each case, the location parameter μ matches the median observation, where the bins are incremented by the CR-39 pixel size in the target plane, approximately 11 μm.

The error bars in Figure 8(c) represent the full width at half-maximum of the fitted distribution at each time. Between 5.6 and 6.6 ns, the median filament spacing is seen to be constant, but the wide error bars on the later measurements do not preclude a continued increase in filament size. The larger error bars on latest time measurement are a product of the large central region where very few protons were detected as shown in the shot number 74471 in Figure 7.

In an interesting experiment by Fox *et al.*,[14] where clear images of the filamentation have been produced, the on-target intensity was significantly lower, 5×10^{13} W/cm^2, probably leading to the lower intra-stream temperatures and increased role of the collisional effects. There have not been any direct measurements of the flow parameters of the type described in Fig. 3. Another morphological difference was a very strong ellipticity of the laser-heated spots on the targets that made the streams initially strongly elongated, with the images taken along this long dimension. In our case, the streams were much closer to axisymmetric, conical flows. As it should be in axisymmetric flows, the proton imaging of the interaction zone in two orthogonal directions in the midplane produced the same images[28] that would not be the case for two highly-elliptical streams.

One issue that has to be remembered in the interpretation of the proton radiographs—in particular, in the experimental evaluation of the characteristic wave-length of the

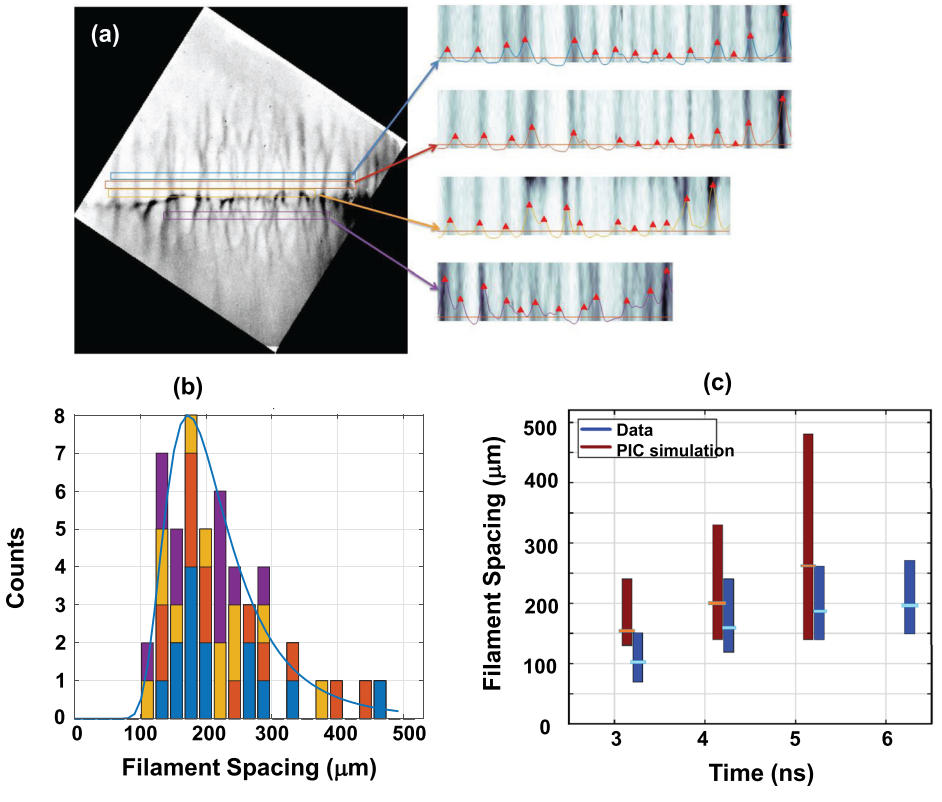

FIG. 8. Calculation of filament spacing in D^{3}He images. (a) Regions of the CR-39 image are selected for analysis. For the 5.6 ns image shown here, regions of interest are shown in different colors. (b) For each region, the mean pixel intensity is calculated per column. The resulting profile is subtracted from the mean pixel value, to produce a 1D profile where the absence of protons (dark regions in the image) correspond to peaks in the profile (colored profiles). Peaks in the profile are identified (red triangles), and the spacing between the peaks is recorded. (b) A histogram of the spacing of the filaments is generated, and the distribution is fit according to Eq. (8). The same analysis is performed for each CR-39 image. (c) Filament spacing as a function of time: data vs. simulation results.

filamentary perturbations—is that the radiograph creates a 2D projection of a 3D structure. Therefore, it may be misleading to identify the wavelength as an average distance between the neighboring structures in Fig. 6. Indeed, consider the situation where the cross-section of the overlap zone of two plasma streams in the mid-plane has a circular shape. It is then obvious that the distance between the centers of filaments seen along the axis may be different from the distance between their axes when projected onto the plane parallel to the system axis. We suggest to name this geometrical effect "a forest effect," by the analogy of evaluating the distance between the trees by looking through a not-too-thick forest from the side and then looking from the top: the number of the trees per unit length for the side view may differ significantly from the actual distance between the tree seen in the top view, and depending strongly on the depth of the forest.

This effect can be particularly significant if the overlap zone is strongly elongated, and the viewing direction is along a long dimension. On the other hand, the elongated interaction zone can allow one to resolve a projection problem by taking projections in two directions, both along and across the zone.

One has also to remember that the filaments are "soft" structures, not the absorbers like the trees in the "forest analogy." The scattering of the protons in the course of propagation through a "forest" of filaments may create additional effects. We leave analysis of these effects for the future work. At the present stage, we simply rely on the synthetic radiographs created in the course of computer simulations (Fig. 9) that look quite similar to the experimentally observed

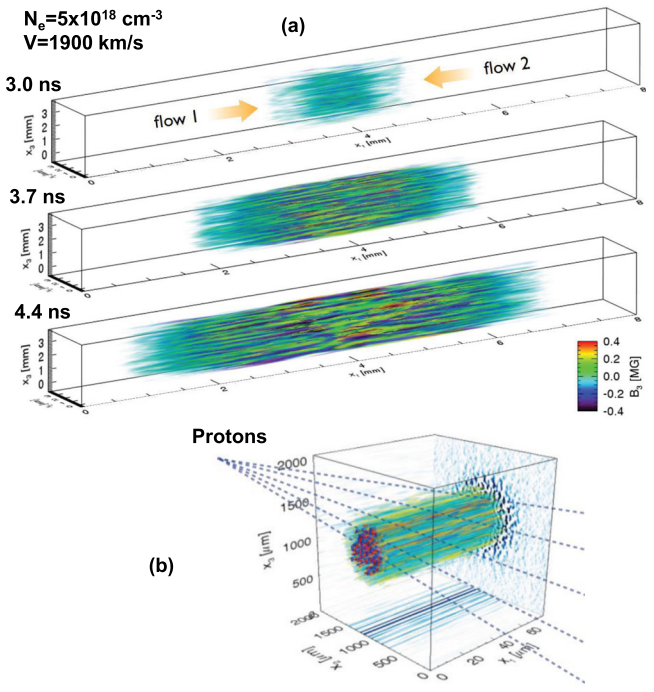

FIG. 9. (a) 3D OSIRIS PIC simulation of interpenetrating flows and the magnetic field generation via Weibel instability. (b) Illustrative geometry of the proton radiography in 3D PIC simulations used to make comparison with the experimental data. The protons probe the self-consistent fields produced in the 3D interaction of the flows and are then projected to the detector.

structures and allow one to compare the geometrical characteristics of both the images and the turbulent field itself.

V. COMPARISON WITH PIC SIMULATION

In order to understand both the Weibel and Biermann battery generated magnetic fields in our proton imaging experimental system, we have conducted detailed 3-dimensional particle-in-cell (3D PIC) simulations of the interaction of the flows and corresponding proton radiography with the code OSIRIS.[33] The code is fully electromagnetic, fully relativistic, and massively parallel, allowing us to capture the relevant physics and scales of the system. We model the interaction of two non-relativistic collisionless counter-streaming plasma flows. The simulation has a size of $(90\,c/\omega_{pi})^3$, uses 2048^3 cells, and 8 particles per cell per species. We consider a flow velocity $v_0 = 0.1\,c$ and use a mass ratio $m_i/Zm_e = 128$. We have tested higher mass ratios and lower velocities in smaller scale 2D simulations obtaining similar results for the evolution of the Weibel instability. However, when using mass ratios below 128, results started to deviate for the time scales of interest for the experiment. A detailed analysis of the simulation results for different conditions will be presented elsewhere.[34] We make use of the scaling relations for a purely electromagnetic instability[18] to scale the simulation results to the plasma parameters measured experimentally at the interaction region: $n_e = 5 \times 10^{18}$ cm^{-3}, $v_e = v_i = 1900$ km/s, $T_e = T_i = 1$ keV. We note that for these plasma conditions, electrons are stable since $v_{the} \gg v_i$, but ions are unstable, $v_{thi} \ll v_i$, leading to the development of the ion Weibel instability.

Figure 9(a) illustrates the evolution of the magnetic field during the interaction region. We observe the clear development of the Weibel instability, with well-defined filaments with k-vector perpendicular to the flow direction. At saturation, the magnetic fields reach amplitudes of 0.4 MG.

To make direct comparison with the experimental diagnostics, we simulated the proton radiographs for the self-consistent field structure. The radiographs were obtained by launching 14.7 MeV protons transversely to the propagation direction of the flow as schematically shown in Figure 9(b). The proton distribution was initialized in OSIRIS following the distribution of an isotropic point source located 1 cm away from the center of the interaction region in order to be fully consistent with our experimental setup. The protons probe the self-consistent fields produced in the 3D simulation and exit on the opposite side of the simulation box, being then propagated ballistically to a square detector of 13 cm × 13 cm placed 30 cm away from the original point source, matching the experimental magnification of 30×. The detector has 512 × 512 points, and ~10^7 probing protons are collected in each image.

In addition to studying the development of the filamentary Weibel structure, we have also performed simulations for the same parameters but where we added the Biermann battery field around the flows that was described in Sec. III. The initial magnetic field amplitude near the interaction region is 0.05 MG. The final proton radiography simulation results are compared with data in Figure 10 showing a

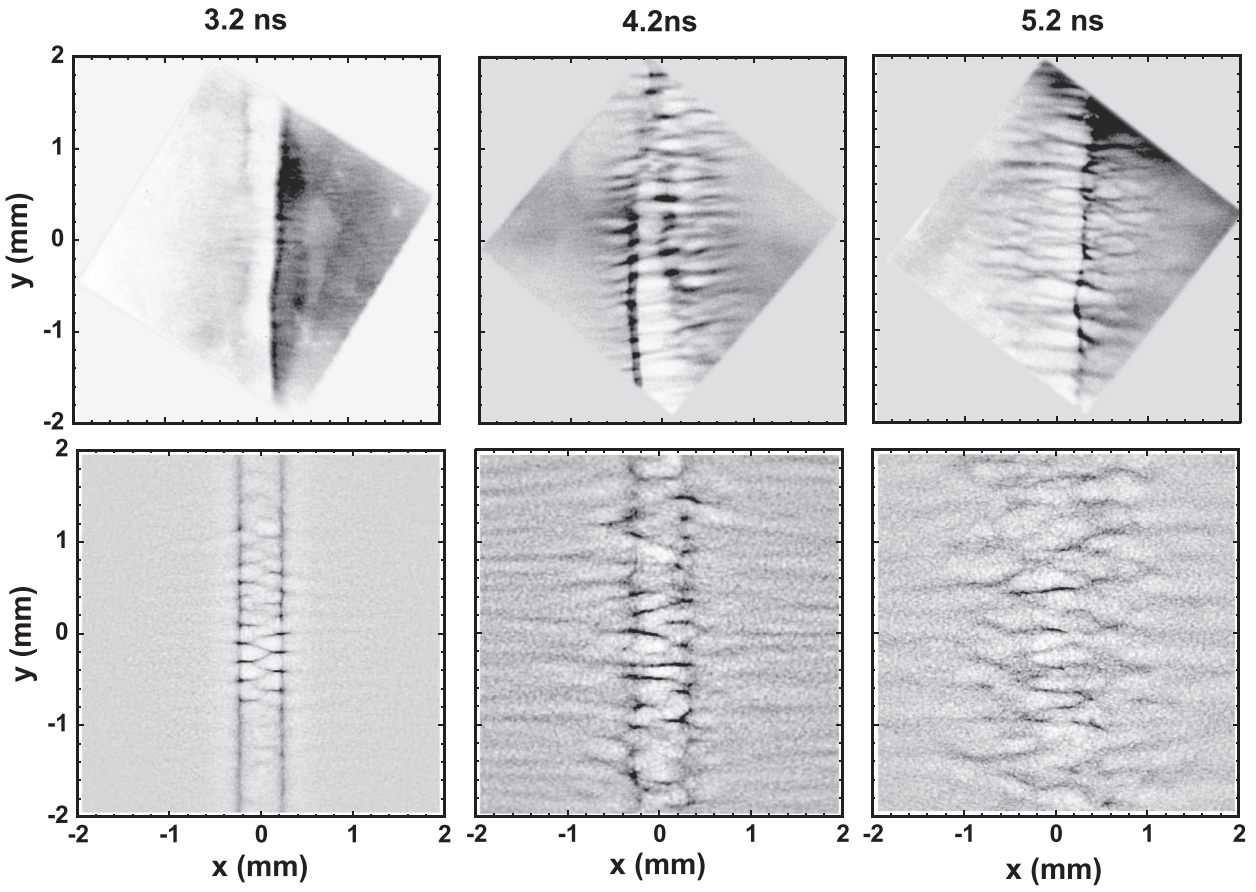

FIG. 10. Comparison between the simulated proton radiography of 3D PIC magnetic fields and the experimental data. Their resemblance are remarkable indicating that the magnetization from the interpenetrating flow was high.

remarkable resemblance. From the detailed studies of simulation and data, we derive the magnetization, which is defined: $\sigma = (B^2/4\pi)/((\gamma - 1)nmc^2)$. This is the fraction of the kinetic energy density converted to magnetic energy density in the system. Figure 11 shows the magnetization obtained in the PIC simulation as a function of time. The dotted line is the field strength without pre-existing magnetic field, whereas the solid line is accounting for the initial field by the Biermann battery. The straight linear line is the theoretical growth rate of the ion Weibel instability. Note that the final total magnetization is 0.01 and the initial Biermann battery field plays no role in the magnetization growth. Thus, Weibel instability filamentation is clearly observed in the laboratory, and a significant self-generated magnetization is indicated.[1] The characteristic Weibel dispersion curves for the experimental results are plotted in Fig. 11(b).

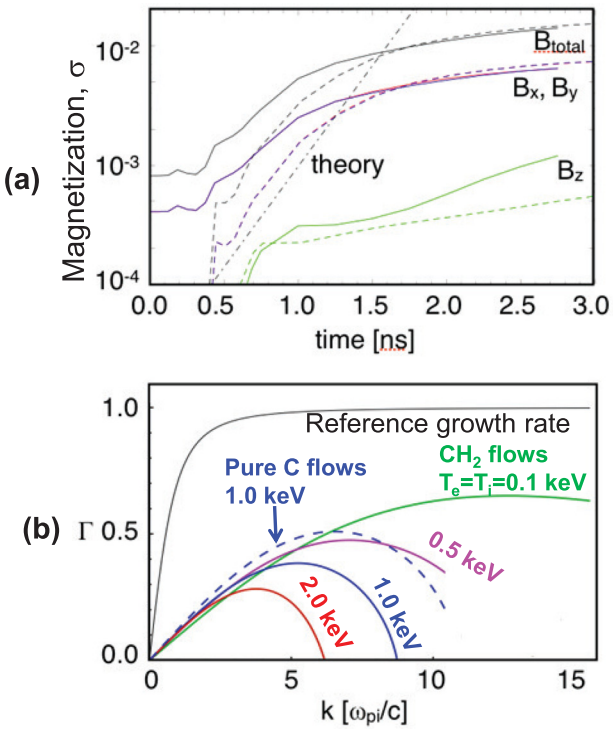

FIG. 11. (a) Magnetization inferred from the PIC simulation. The data indicate that we achieved upto 1% magnetization. (b) Characteristic dispersive curve of Weibel growth rate vs. the wave number at different electron and ion temperatures of 0.1 keV (green), 0.5 keV (magenta), 1 keV (blue), and 2 keV (red). Reprinted with permission from Nat. Phys. **11**, 173 (2015). Copyright 2015 Nature Publishing Group.

VI. WEIBEL THEORY AND DISCUSSION

A. Weibel modes in relation to our experiment

The Weibel instability has been first considered for the electron plasma with anisotropic electron distribution.[7,35] This was a purely electron mode, with the ions forming a uniform background. The mode has a peculiar feature: its growth rate is anisotropic, strongly favoring the modes with the wave-vector perpendicular to the axis of symmetry of the electron distribution. As directions (x, y) in the plane

perpendicular to the axis of symmetry (z) are equivalent, the modes acquire a characteristic filamentary structure, with the filaments parallel to z. The modes are electromagnetic, with significant perturbation of the magnetic field.

Later, the similar electromagnetic modes have been analyzed in a variety of settings, including the modes driven by relativistic counter-streaming electron and positron plasmas[3,9] and the modes driven by counter-streaming ion flows.[21] It is the latter, ion-driven version that is thought to be responsible for the collisionless shock generation in a non-relativistic electron-ion plasma and that is a focus of the present study.

The linear theory of the collisionless Weibel instability driven by the collisionless counter-streaming plasmas is well developed and summarized, in particular, in Refs. 15 and 37. For the experiments of the type performed in our study, one may need to consider a collisional version of the Weibel instability, where the inter-stream ion collisions are negligibly rare, but intra-stream collisions are important.[18] Especially significant can be the collisions in the electron background that may cause decrease of the growth rates. These collisional effects have been described in Ref. 18. To make collisional effect insignificant, one has to take special care of working in the regimes of high electron temperatures, and this condition was satisfied in our experiments. This is an important point, as a low collisionality is typical for the astrophysical environment which we are imitating.

In our experiment, there exists a regular magnetic field generated, most probably, by the Biermann battery effect.[37] It was found experimentally[38] by the proton deflectometry technique and explained theoretically as being generated at the targets by the Biermann battery effect and advected to the midplane.[39] The magnitude of this field is probably in the range of a few T.[28,39] The field is azimuthal (the field lines encircle the axis) and has opposite polarities at the opposite sides of the midplane. The "thickness" of the zone of the enhanced field is about 0.5 mm on each side of the midplane; between these two zones, the field reversal occurs in the layer also about 0.5 mm thick.

The gyroradius of 1000 km/s carbon ions in the 4 Tesla field is $\rho_i \sim 5$ mm, i.e., significantly larger than the thickness of the enhanced field zones. As the "kicks" that the ions experience when passing these two zones have opposite directions, the net effect is very minimal (essentially zero near the axis). The situation is quite different for the electrons: the gyroradius of 1 keV electrons in the 4 Tesla field is $\rho_e \sim 25\,\mu$m. This may have an effect on the electron stabilizing terms in the dispersion relation for the Weibel instability, for the modes with $k\rho_e < 1$, i.e., for the wavelengths $\lambda > 2\pi\rho_e \approx 150\,\mu$m. As the observed wavelengths are in this range, the presence of the electron magnetization may have a favorable effect on the instability development. On the other hand, the regular magnetic field encircling the axis is zero on the axis itself as well as between the magnetic "pancakes" of Fig. 5, whereas the observed filamentary structures in Fig. 6 occupy both zones. So, the presence of the regular magnetic field is not a factor strongly affecting the instability, although, possibly, somewhat enhancing it.

The observed filamentary structures are localized near the midplane, extending in the axial direction somewhat beyond the Biermann battery "pancakes." The length of the filaments is much larger than the distance between them, i.e., a condition

$$k_{\|} \ll k_{\perp} \tag{9}$$

is satisfied, with $k_{\|}$ and $k_{\perp}$ being the components of the wave vector parallel and perpendicular to the vector of the relative velocity of the flows. An axial extent of the filaments near the equatorial plane is about ten of their radial wavelengths (see Fig. 8(a)). The radial extent of the zone occupied by the filaments is a few millimeters.

B. Assessing a global structure of the filamentation zone

In this section, we identify the factors that could explain the geometry of the filamentation zone: lower growth rates at larger distances from it; the effects of advection; and the velocity-shear stabilization. In the attempt to evaluate the role of these factors, we have performed a linear stability analysis accounting for the spatially varying density of each stream and spatially varying directions of their flow velocities. As the experimentally observed wavelengths of perturbations are small compared to the global scale of the experiment, an eikonal approach is sufficient for the evaluation of the local growth rate.

We denote the ion densities and velocities of each stream as $n_{1,2}$ and $\boldsymbol{v_{1,2}}$. Switching to the frame moving with the average velocity

$$\boldsymbol{u} = \frac{n_1 \boldsymbol{v_1} + n_2 \boldsymbol{v_2}}{n_1 + n_2}, \tag{10}$$

we find that in the frame moving with velocity $\boldsymbol{u}$, the streams are counter-propagating, with velocities

$$\boldsymbol{v'_{1,2}} = \boldsymbol{v_{1,2}} - \boldsymbol{u} = \pm(\boldsymbol{v_1} - \boldsymbol{v_2})\frac{n_{1,2}}{n_1 + n_2}. \tag{11}$$

In this frame, a canonical derivation of the Weibel dispersion relation for the modes propagating in the perpendicular direction to the flows[15,21,22,36] yields the following dispersion relation for the growth-rate Γ (see derivation in the Appendix)

$$\Gamma^2 = \frac{k^2 w^2}{1 + k^2 c^2/\omega_{pi}^2}; \quad w^2 \equiv \frac{n_1 n_2}{(n_1 + n_2)^2}(\boldsymbol{v}_1 - \boldsymbol{v}_2)^2, \tag{12}$$

with ω_{pi} being an ion plasma frequency corresponding to the total ion density

$$\omega_{pi}^2 = \frac{4\pi Z^2 (n_1 + n_2) e^2}{A m_p}. \tag{13}$$

In Eq. (12), we have neglected a stabilizing electron term that is insignificant for the sufficiently hot electrons and is further reduced by the presence of the regular magnetic field.

The growth rate Γ increases with the wave number and reaches saturation at

$$k \sim k_0 \equiv \frac{\omega_{pi}}{c}. \tag{14}$$

It is usually assumed that this is a representative wave number for the filaments, determining their transverse size. The saturation level of the growth-rate (denoted as Γ^*) is:

$$\Gamma^* = \omega_{pi}\frac{w}{c}. \tag{15}$$

This corresponds to the plateau on the curve labelled as "Reference growth rate" in Fig. 11(b). In order for the instability to develop from the initial noise to the level where the Weibel filaments would become visible by our diagnostic tools, Γ^* (15) should be significantly higher than the inverse duration of the interaction, as well as: (i) the inverse time of the plasma advection from the high growth-rate zone; (ii) the shearing rate (see below).

In order to find out how Γ^* (15) varies over the interaction domain between the two foils, we choose a model of two identical streams originating at the opposite targets separated by a distance $2L$ (so that L is the distance from the center of the interaction region to each of the targets), see Figure 12. As the laser spots on the targets are small compared to L, we assume that we have point sources, so that velocity of each stream at some point is directed along the line connecting the observation point to the origin of this stream. The sources of the streams are assumed to be identical; the density in each stream is inversely proportional to the square of the distance from the corresponding source.

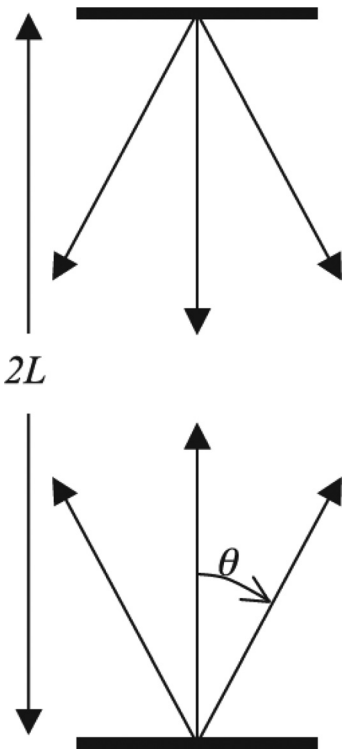

FIG. 12. The geometry of the model. The velocity of the stream, v, at each point is parallel to the line connecting this point with the point source; the density scales inversely proportional to the square of the distance to the source (a steady flow with a constant velocity).

C. Advective, shear, and scattering stabilization

The growth rate (15) is a result of maximizing the growth-rate over k at each spatial point. This maximum (over k) growth rate itself varies in space. We need to quantify this variation in order to see whether there is a strong peaking of the Γ^* near the midplane. For our flow model of two identical divergent streams emerging from the laser-heated areas on the foils, the spatial maximum of the growth rate (15) is situated in the center. The overall spatial dependence of Γ^* is shown in Fig. 13 (mind the horizontal orientation of the targets). This figure shows that the growth rate is near maximum over a very large region (see, e.g., a 0.8 contour). This is not what would correspond to the spatial distribution of the modes observed experimentally. So, we consider below, other limiting factors, those associated with advection and flow shearing.

Figure 14 shows the streamlines of the advection flow. The flow moves the perturbations in the general direction towards the midplane. This may explain the absence of the filaments, say, halfway between the target and the midplane, despite essentially the same growth-rate. The advection velocity is zero near the center and grows along the axial coordinate. One can apply the same explanation to the radial size of the filamentation zone: the advection velocity increases in the radial direction and may advect perturbations away from the zone of a high growth-rate. This may set the limit to the radial extent of the zone with large perturbations. On the other hand, the advection alone seems to be insufficient, because the instability e-folding time $1/\Gamma^*$ is much shorter than the radial advection time which is a few r/v, with v being a velocity of an individual jet. For the electron density of $10^{19} cm^{-3}$ and $v = 10^8 cm/s$, the e-folding time is $\sim 10^{-10} s$, whereas the radial advection time is much longer $\sim (2-3) \times 10^{-9} s$.

A rough estimate of the flow shear across the long direction of the filaments evaluated according to the explanations given in Fig. 14 is $S \sim v/L \sim 2 \times 10^8 s^{-1}$. The shear causes a rapid growth of the parallel wave number. In the eikonal approximation, this growth is described by equation[40]

$$\dot{k}_{\|} = k_{\perp} S. \tag{16}$$

Within the growth time $1/\Gamma$, the parallel wave-number changes by

$$\Delta k_{\|}/k_{\|} \sim (k_{\perp}/k_{\|})(S/\Gamma) \sim 10 S/\Gamma. \tag{17}$$

If the thus evaluated $\Delta k_{\|}/k_{\|}$ exceeds unity, this means that the parallel wave number increases faster than the growth of perturbations occurs, leading to the suppression of the instability. The condition $10S/\Gamma > 1$ can be satisfied even for $\Gamma \sim \Gamma^*$. This effect can potentially explain the observed localization features of the filamentary structure near the midplane, with a finite radial extent. Here, we have used the simplest version of the shear stabilization concept. A more complete analysis can be developed using the basic references.[41–43]

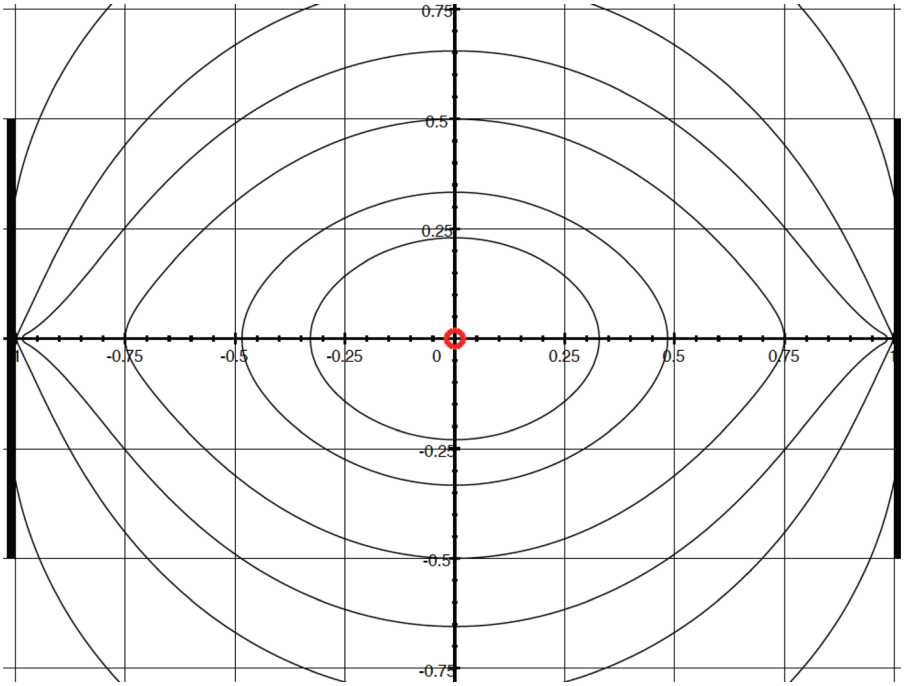

FIG. 13. The spatial dependence of the growth-rate Γ^* normalized to its maximum situated at the center (red dot). Γ^* is defined by Equation (15). The contours (starting from inside) correspond to the growth rates 0.95. 0.9, 0.8, 0.7, 0.6, and 0.5.

Finally, an axial localization may also be affected by the ion scattering on the perturbations present near the midplane. Each of the two of the ion streams leaves this zone having experienced some scattering that introduces an effective "temperature" of the ions leaving the interaction zone. Then, outside the interaction zone, the "heated" streams propagate through the unperturbed ones. This creates a peculiar situation of the interaction of cold and warm streams. As the ion thermal spread reduces the growth rate in the symmetric streams (see Fig. 11(b)), one may expect a similar effect when only one stream is heated. We leave detailed analysis of the shear and scattering stabilization for future work.

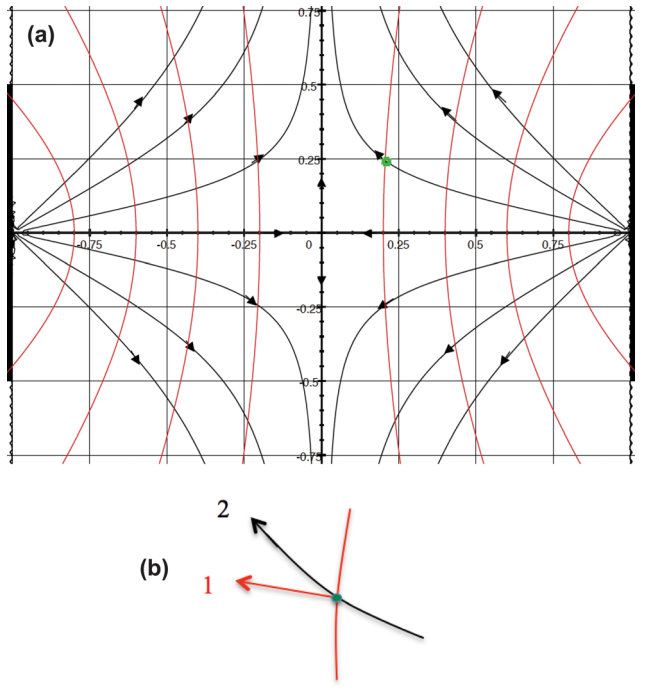

FIG. 14. Streamlines and shearing: (a) Streamlines of the advection flow Eq. (10) are shown in black. Arrows show the direction of the flow. Red lines represent cross-sections of the surfaces normal to the direction of the relative velocity $v_1 - v_2$. The Weibel filaments are aligned with $v_1 - v_2$ and therefore normal to these surfaces. (b) Towards evaluation of the shear: shown is an enlarged vicinity of a point shown in green in panel a; the direction of the filaments is shown by an arrow 1 normal to the red surface; to find the shear S, one has to take a projection of the advection velocity 2 to the red surface and find the derivative of this projection along the normal 1.

VII. CONCLUSION

In conclusion, laser generated counter-streaming plasma flows have been studied in connection to astrophysical collisionless shocks. We observe that the intra-collisional electron-ion interaction by electron-drag force elevates the electron temperature and electrostatic instabilities raise the ion temperatures for the double flows. We detect very stable

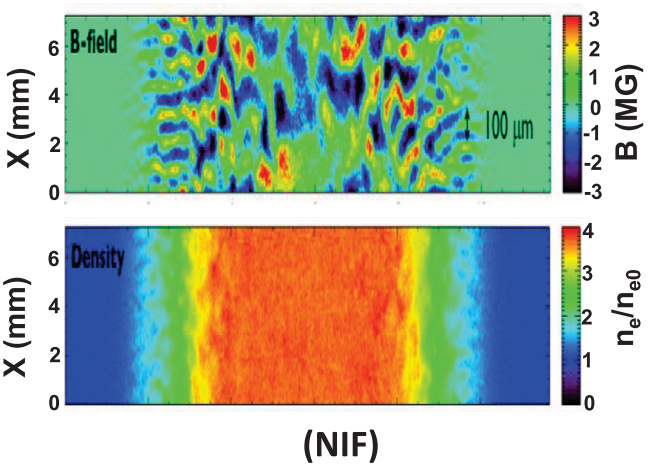

FIG. 15. 3D PIC simulation results of B-field (top) and electron density (bottom) for the NIF experiments. We anticipate that the NIF experiments will be able to produce fully formed collisionless shocks ($n_e/n_{e0} \sim 4$) and B field near 3 MG.

self-organizing field structures that originate from the recompression of the advected Biermann battery magnetic field. The Weibel filamentation is directly imaged, and a magnetization level of 1% is derived.

While these results are very unique, the Omega experiments did not reach the instability scale length that is required to generate a fully formed shock. The NIF experiment will be able to create true Weibel mediated collisionless shocks, as indicated in Figure 15 by the PIC simulation, where the density is predicted to be four times the initial density and the magnetic field to be up to 300 Tesla. Observation of this high level of magnetization will provide a direct connection of astrophysical magnetic field generation to the subsequent shock formation.

ACKNOWLEDGMENTS

This work was performed under the auspices of the U.S. Department of Energy by Lawrence Livermore National Laboratory under Contract DE-AC52-07NA27344.

APPENDIX: DERIVATION OF THE DISPERSION RELATION

In the frame moving with velocity (10), we have two ion streams propagating towards each other with velocities

$$\boldsymbol{v_1'} = \boldsymbol{v_0}\frac{n_2}{n_1+n_2}; \quad \boldsymbol{v_2'} = -\boldsymbol{v_0}\frac{n_1}{n_1+n_2} \tag{A1}$$

(we have chosen their common direction as an axis z, with $\boldsymbol{v}_0$ being the absolute value of $(\boldsymbol{v}_1 - \boldsymbol{v}_2)$. The perturbation wave vector k is directed along axis x, the magnetic field perturbation along axis y, and the current and electric field perturbations along axis z. The ions are assumed to have negligible thermal spread. The electrons form a uniform resting background in the unperturbed state.

The current perturbation consist of the ion and electric components, $\delta j_z = \delta j_{zi} + \delta j_{ze}$ with

$$\delta j_{zi} = Ze(v_1'\delta n_1 + v_2'\delta n_2 + n_1\delta v_{z1} + n_2\delta v_{z2}). \tag{A2}$$

The beam density perturbations are related to the x components of their velocity perturbations by the continuity equations

$$\Gamma\delta n_{1,2} + ikn_{1,2}\delta v_{x1,2} = 0, \tag{A3}$$

where Γ is a complex growth rate (It turns out that in the frame that we have chosen, it is real, i.e., the perturbation growth is purely exponential.) For brevity, we used here notation k for the perpendicular component of the wave vector; we also assumed that the parallel component is negligibly small (this corresponds to the fastest growth of perturbations). The velocity perturbations are found from the ion momentum equation:

$$\delta v_{x1,2} = -\frac{Zev_{1,2}'}{Am_p\Gamma}\delta B_y, \tag{A4}$$

$$\delta v_{z1,2} = \frac{Ze}{Am_p\Gamma}\delta E_z. \tag{A5}$$

Note that Equations (A1), (A3), and (A4) show that the ion density perturbation is zero, $\delta n_1 + \delta n_2 = 0$, similar to what takes place in the symmetric (equal density) flows.[22] Relating the electric and magnetic field perturbations by the Faraday equation, $ik\delta E_z = \Gamma\delta B_y/c$, and using Eqs. (A3)–(A5), we obtain the following relation between the magnetic field and ion current perturbations:

$$\delta j_{zi} = \frac{ikZ^2e^2}{Am_pc}\left(\frac{n_1v_1'^2 + n_2v_2'^2}{\Gamma^2} - \frac{1}{k^2}\right)\delta B_y. \tag{A6}$$

The last term in the right-hand side plays a stabilizing role, reducing the current perturbation. To find a dispersion relation, one has to add the electron current perturbation and use the Ampere law, $ik\delta B_y = 4\pi\delta j_z/c$. This yields the following equation:

$$\left[1 - \frac{4\pi Z^2e^2}{Am_pc^2}\left(\frac{n_1v_1'^2 + n_2v_2'^2}{\Gamma^2} - \frac{1}{k^2}\right)\right]\delta B_y = -\frac{4\pi i}{kc}\delta j_{ze}. \tag{A7}$$

For brevity, we used here notation k for the perpendicular component of the wave vector; we also assumed that the parallel component is negligibly small. The isotropic electron gas is not perturbed by the magnetic field perturbation, but it reacts on the presence of an electric field δE_z. As the electron inertia is very small, the electrons would essentially cancel the ion current perturbation if not the presence of thermal stabilization effect in a collisionless case. The essence of this effect is that the electron thermal motion in the x direction causes them to average and significantly reduce their response to the electric field perturbation. Any effect that would suppress the electron current acts in the same direction, including the magnetic field perpendicular to the ion streams direction. An expression for the electron response where both collisional and collisionless effects have been included can be found in Ref. 22. In this article, in order to illustrate the possible significance of the velocity shear of the composite flow and, possibly, advection for the stabilization of the Weibel instability, we have considered the case where the stabilizing electron response is small, and dropped the right-hand side in Eq. (A7). The remaining part then immediately yields Eq. (12).

[1]C. M. Huntington, F. Fiuza, J. S. Ross, A. B. Zylstra, R. P. Drake, D. H. Froula, G. Gregori, N. L. Kugland, C. C. Kuranz, M. C. Levy, C. K. Li, J. Meinecke, T. Morita, R. Petrasso, C. Plechaty, B. A. Remington, D. D. Ryutov, Y. Sakawa, A. Spitkovsky, H. Takabe, and H.-S. Park, "Observation of magnetic field generation via the weibel instability in interpenetrating plasma flows," Nat. Phys. **11**, 173–176 (2015).
[2]D. W. Forslund and C. R. Shonk, "Formation and structure of electrostatic collisionless shocks," Phys. Rev. Lett. **25**, 1699 (1970).
[3]M. V. Medvedev and A. Loeb, "Generation of magnetic fields in the relativistic shock of gamma-ray burst sources," Astrophys. J. **526**, 697–706 (1999).
[4]R. Schlickeiser and P. K. Shukla, "Cosmological magnetic field generation by the Weibel instability," Astrophys. J. **599**, L57–L60 (2003).

[5]P. Chang, A. Apitkovsky, and J. Arons, "Long-term evolution of magnetic turbulence in relativistic collisionless shocks," Astrophys. J. **674**, 378–387 (2008), e-print arXiv:0801.4583.
[6]A. Bret, "Weibel, two-stream, filamentation, oblique, bell, buneman. Which one grows faster?," Astrophys. J. **699**, 990 (2009).
[7]E. S. Weibel, "Spontaneously growing transverse waves in a plasma due to an anisotropic velocity distribution," Phys. Rev. Lett. **2**, 83–84 (1959).
[8]J.-I. Sakai, R. Schlickeiser, and P. Shukla, "Simulation studies of the magnetic field generation in cosmological plasmas," Phys. Lett. A **330**, 384–389 (2004).
[9]A. Spitkovsky, "On the structure of relativistic collisionless shocks in electron-ion plasmas," Astrophys. J. Lett. **673**, L39–L42 (2008).
[10]M. V. Medvedev and O. V. Zakutnyaya, "Magnetic fields and cosmic rays in grbs: A self-similar collisionless foreshock," Astrophys. J. **696**, 2269 (2009).
[11]M. V. Medvedev, L. O. Silva, M. Fiore, R. A. Fonseca, and W. B. Mori, "Generation of magnetic fields in cosmological shocks," J. Korean Astron. Soc. **37**, 533–541 (2004).
[12]T. N. Kato and H. Takabe, "Electrostatic and electromagnetic instabilities associated with electrostatic shocks: Two-dimensional particle-in-cell simulation," Phys. Plasmas **17**, 032114 (2010).
[13]A. Spitkovsky, "Simulations of relativistic collisionless shocks: shock structure and particle acceleration," AIP Conf. Proc. **801**, 345–350 (2005).
[14]W. Fox, G. Fiksel, A. Bhattacharjee, P.-Y. Chang, K. Germaschewski, S. X. Hu, and P. M. Nilson, "Filamentation instability of counterstreaming laser-driven plasmas," Phys. Rev. Lett. **111**, 225002 (2013).
[15]R. P. Drake and G. Gregori, "Design considerations for unmagnetized collisionless-shock measurements in homologous flows," Astrophys. J. **749**, 171 (2012).
[16]H.-S. Park, D. Ryutov, J. Ross, N. Kugland, S. Glenzer, C. Plechaty, S. Pollaine, B. Remington, A. Spitkovsky, L. Gargate, G. Gregori, A. Bell, C. Murphy, Y. Sakawa, Y. Kuramitsu, T. Morita, H. Takabe, D. Froula, G. Fiksel, F. Miniati, M. Koenig, A. Ravasio, A. Pelka, E. Liang, N. Woolsey, C. Kuranz, R. Drake, and M. Grosskopf, "Studying astrophysical collisionless shocks with counterstreaming plasmas from high power lasers," High Energy Density Phys. **8**, 38–45 (2012).
[17]J. S. Ross, S. H. Glenzer, P. Amendt, R. Berger, L. Divol, N. L. Kugland, O. L. Landen, C. Plechaty, B. Remington, D. Ryutov, W. Rozmus, D. H. Froula, G. Fiksel, C. Sorce, Y. Kuramitsu, T. Morita, Y. Sakawa, H. Takabe, R. P. Drake, M. Grosskopf, C. Kuranz, G. Gregori, J. Meinecke, C. D. Murphy, M. Koenig, A. Pelka, A. Ravasio, T. Vinci, E. Liang, R. Presura, A. Spitkovsky, F. Miniati, and H.-S. Park, "Characterizing counter-streaming interpenetrating plasmas relevant to astrophysical collisionless shocks," Phys. Plasmas **19**, 056501 (2012).
[18]D. D. Ryutov, N. L. Kugland, H.-S. Park, C. Plechaty, B. A. Remington, and J. S. Ross, "Intra-jet shocks in two counter-streaming, weakly collisional plasma jets," Phys. Plasmas **19**, 074501 (2012).
[19]B. A. Trubnikov, "Particle interactions in a fully ionized plasma," in *Reviews of Plasma Physics*, edited by M. A. Leontovich (Consultants Bureau, NY, 1965), Vol. 1, p. 105.
[20]A. A. Vedenov and D. D. Ryutov, "Quasilinear effects in two-stream instabilities," in *Reviews of Plasma Physics*, edited by M. A. Leontovich (Consultants Bureau, NY, 1975), Vol. 6, p. 1.
[21]T. N. Kato and H. Takabe, "Nonrelativistic collisionless shocks in unmagnetized electron-ion plasmas," Astrophys. J. Lett. **681**, L93–L96 (2008).
[22]D. D. Ryutov, F. Fiuza, C. M. Huntington, J. S. Ross, and H.-S. Park, "Collisional effects in the ion weibel instability for two counter-propagating plasma streams," Phys. Plasmas **21**, 032701 (2014).
[23]T. R. Boehly, R. S. Craxton, T. H. Hinterman, J. H. Kelly, T. J. Kessler, S. A. Kumpan, S. A. Letzring, R. L. McCrory, S. F. B. Morse, W. Seka, S. Skupsky, J. M. Soures, and C. P. Verdon, "The upgrade to the omega laser system," Rev. Sci. Instrum. **66**, 508–510 (1995).
[24]J. S. Ross, S. H. Glenzer, J. P. Palastro, B. B. Pollock, D. Price, G. R. Tynan, and D. H. Froula, "Thomson-scattering measurements in the collective and noncollective regimes in laser produced plasmas (invited)," Rev. Sci. Instrum. **81**, 10D523 (2010).
[25]J. S. Ross, H.-S. Park, R. Berger, L. Divol, N. L. Kugland, W. Rozmus, D. Ryutov, and S. H. Glenzer, "Collisionless coupling of ion and electron temperatures in counterstreaming plasma flows," Phys. Rev. Lett. **110**, 145005 (2013).
[26]S. C. Wilks, A. B. Langdon, T. E. Cowan, M. Roth, M. Singh, S. Hatchett, M. H. Key, D. Pennington, A. MacKinnon, and R. A. Snavely, "Energetic proton generation in ultra-intense laser–solid interactions," Phys. Plasmas **8**, 542–549 (2001).
[27]C. K. Li, F. H. Seguin, J. A. Frenje, J. R. Rygg, R. D. Petrasso, R. P. J. Town, P. A. Amendt, S. P. Hatchett, O. L. Landen, A. J. Mackinnon, P. K. Patel, V. A. Smalyuk, J. P. Knauer, T. C. Sangster, and C. Stoeckl, "Monoenergetic proton backlighter for measuring E and B fields and for radiographing implosions and high-energy density plasmas (invited)," Rev. Sci. Instrum. **77**, 10E725 (2006).
[28]N. L. Kugland, J. S. Ross, P.-Y. Chang, R. P. Drake, G. Fiksel, D. H. Froula, S. H. Glenzer, G. Gregori, M. Grosskopf, C. Huntington, M. Koenig, Y. Kuramitsu, C. Kuranz, M. C. Levy, E. Liang, D. Martinez, J. Meinecke, F. Miniati, T. Morita, A. Pelka, C. Plechaty, R. Presura, A. Ravasio, B. A. Remington, B. Reville, D. D. Ryutov, Y. Sakawa, A. Spitkovsky, H. Takabe, and H.-S. Park, "Visualizing electromagnetic fields in laser-produced counter-streaming plasma experiments for collisionless shock laboratory astrophysics," Phys. Plasmas **20**, 056313 (2013).
[29]A. B. Zylstra, C. K. Li, H. G. Rinderknecht, F. H. Séguin, R. D. Petrasso, C. Stoeckl, D. D. Meyerhofer, P. Nilson, T. C. Sangster, S. Le Pape, a. Mackinnon, and P. Patel, "Using high-intensity laser-generated energetic protons to radiograph directly driven implosions," Rev. Sci. Instrum. **83**, 013511 (2012).
[30]C. K. Li, F. H. Séguin, J. R. Rygg, J. A. Frenje, M. Manuel, R. D. Petrasso, R. Betti, J. Delettrez, J. P. Knauer, F. Marshall, D. D. Meyerhofer, D. Shvarts, A. A. Smalyuk, C. Stoeckl, O. L. Landen, R. P. J. Town, C. A. Back, and J. D. Kilkenny, "Monoenergetic-Proton-Radiography Measurements of Implosion Dynamics in Direct-Drive Inertial-Confinement Fusion," Phys. Rev. Lett. **100**(22), 225001 (2008).
[31]F. H. Seguin, J. A. Frenje, C. K. Li, D. G. Hicks, S. Kurebayashi, J. R. Rygg, B.-E. Schwartz, R. D. Petrasso, S. Roberts, J. M. Soures, D. D. Meyerhofer, T. C. Sangster, J. P. Knauer, C. Sorce, V. Y. Glebov, C. Stoeckl, T. W. Phillips, R. J. Leeper, K. Fletcher, and S. Padalino, "Spectrometry of charged particles from inertial-confinement-fusion plasmas," Rev. Sci. Instrum. **74**, 975–995 (2003).
[32]N. L. Kugland, D. D. Ryutov, C. Plechaty, J. S. Ross, and H.-S. Park, "Invited article: Relation between electric and magnetic field structures and their proton-beam images," Rev. Sci. Instrum. **83**, 101301 (2012).
[33]R. Fonseca, L. Silva, F. Tsung, V. Decyk, W. Lu, C. Ren, W. Mori, S. Deng, S. Lee, T. Katsouleas, and J. Adam, "Osiris: A three-dimensional, fully relativistic particle in cell code for modeling plasma based accelerators," in *Computational Science, ICCS 2002*, Lecture Notes in Computer Science Vol. 2331, edited by P. Sloot, A. Hoekstra, C. Tan, and J. Dongarra (Springer Berlin/Heidelberg, 2002), pp. 342–351.
[34]F. Fiuza *et al.*, "A three-dimensional particle in cell simulation for collisionless shock experiments," (private communication).
[35]B. D. Fried, "Mechanism for instability of transverse plasma waves," Phys. Fluids **2**, 337 (1959).
[36]R. C. Davidson, D. A. Hammer, I. Haber, and C. E. Wagner, "Nonlinear development of electromagnetic instabilities in anisotropic plasmas," Phys. Fluids **15**, 317–333 (1972).
[37]L. Biermann, "Über den upsprung der magnetfelder auf sternen und im interstellaren raum," Z. Naturforschung **5**, 65–71 (1950).
[38]N. L. Kugland, D. D. Ryutov, P.-Y. Chang, R. P. Drake, G. Fiksel, D. H. Froula, S. H. Glenzer, G. Gregori, M. Grosskopf, M. Koenig, Y. Kuramitsu, C. Kuranz, M. C. Levy, E. Liang, J. Meinecke, F. Miniati, T. Morita, A. Pelka, C. Plechaty, R. Presura, A. Ravasio, B. A. Remington, B. Reville, J. S. Ross, Y. Sakawa, A. Spitkovsky, H. Takabe, and H.-S. Park, "Self-organized electromagnetic field structures in laser-produced counter-streaming plasmas," Nat. Phys. **8**, 809–812 (2012).
[39]D. D. Ryutov, N. L. Kugland, M. C. Levy, C. Plechaty, J. S. Ross, and H. S. Park, "Magnetic field advection in two interpenetrating plasma streams," Phys. Plasmas **20**, 032703 (2013).
[40]L. D. Landau and E. M. Lifshitz, *Fluid Mechanics* (Pergamon, NY, 1987).
[41]P. H. Diamond, S.-I. Itoh, K. Itoh, and T. S. Hahm, "Zonal flows in plasma review," Plasma Phys. Controlled Fusion **47**, R35–R161 (2005).
[42]N. F. Loureiro, A. A. Schekochihin, K. College, and S. C. Cowley, "Instability of current sheets and formation of plasmoid chains," Phys. Plasmas **14**, 18–22 (2007), e-print arXiv:0703631 [astro-ph].
[43]L. Ni, K. Germaschewski, Y. M. Huang, B. P. Sullivan, H. Yang, and A. Bhattacharjee, "Linear plasmoid instability of thin current sheets with shear flow," Phys. Plasmas **17**, 052109 (2010).